coatings

MDPI

Article

Examination of Oxide Formation in Oxidation of Inconel 600 and 625 at High Temperatures Using Phase Diagrams

Dong-Hyuk Kim [1], Jaegu Choi [1] and Seong-Ho Ha [2,*]

[1] Advanced Mobility Components Group, Korea Institute of Industrial Technology, Daegu 42994, Republic of Korea; dhkim76@kitech.re.kr (D.-H.K.); jgchoi@kitech.re.kr (J.C.)
[2] Materials Supply Chain R&D Department, Korea Institute of Industrial Technology, Incheon 21999, Republic of Korea
* Correspondence: shha@kitech.re.kr

Abstract: Effects of main and trace elements on the formation of oxide in the oxidation behavior of Inconel 600 and 625 were investigated in this study using various calculated phase diagrams. After the isothermal oxidation tests at 1000 and 1100 °C, Nickel 201 for comparison showed significant growth of an oxide layer corresponding to NiO, and the NiO layer consisted of oxide crystals with both equiaxed and columnar shapes. As the temperature increased, the growth of the oxide layer proceeded mainly through columnar crystals. On the other hand, Inconel 600 and 625 showed relatively thin oxide layers, which were confirmed to be mainly composed of Cr_2O_3. The Cr_2O_3 layer was composed of equiaxed fine crystals. In the case of Inconel 625, an intermediate layer was formed at the interface between Cr_2O_3 and the base metal. It was found that the surface segregation of Cr as the main alloying element influenced the formation of the oxide layer of two Inconel alloys, and that some elements disappeared from the base metal near the surface due to continuous surface segregation and vaporization. On the other hand, even some elements with trace amounts showed strong surface segregation and contributed to the formation of oxide layer.

Keywords: Inconel 600; Inconel 625; oxidation; Cr_2O_3; phase diagram; electron backscatter diffraction

check for updates

Citation: Kim, D.-H.; Choi, J.; Ha, S.-H. Examination of Oxide Formation in Oxidation of Inconel 600 and 625 at High Temperatures Using Phase Diagrams. *Coatings* **2024**, *14*, 1550. https://doi.org/10.3390/coatings14121550

Academic Editor: Rodrigo da Silva

Received: 10 October 2024
Revised: 2 December 2024
Accepted: 9 December 2024
Published: 11 December 2024

Copyright: © 2024 by the authors. Licensee MDPI, Basel, Switzerland. This article is an open access article distributed under the terms and conditions of the Creative Commons Attribution (CC BY) license (https://creativecommons.org/licenses/by/4.0/).

1. Introduction

Ni-based superalloys are high-temperature-resistant alloys typically used for the parts that encounter temperatures above 500 °C due to their exceptional mechanical properties, lower thermal expansion coefficients, and higher oxidation resistance than stainless steel parts. A wide range of chemical compositions are considered in nickel-based superalloys since their oxidation behaviors are complex [1,2]. Inconel alloys are Ni-based alloys which mainly consist of various combinations of Cr and Fe, as well as smaller amounts of W, Mo, Ta, Nb, Ti, and Al. Trace amounts of alloying elements such as Mn, Si, C, Cu, etc., are also included [3]. Inconel 600 and Inconel 625 are Ni-based alloys with superior corrosion resistance and high temperature properties, which determine their widespread applications in aeronautical, aerospace, marine, and nuclear industries.

Inconel 600 is widely used for applications that require resistance to corrosion and heat. The various advantages of Inconel 600 has led to its use in many applications involving temperatures from cryogenic to above 1100 °C. Its strength, corrosion resistance, and oxidation resistance at high temperature make it useful in the chemical industry, the heat-treating industry, as well as the aeronautical field [4,5]. It is also a good material for the construction of nuclear reactors due to its excellent resistance to corrosion in high-purity water. Inconel 625 has also received extensive attention for their outstanding properties including high tensile and creep strengths and excellent corrosion and oxidation resistance in different mediums [6,7]. These properties allow it to be widely applied in various sectors associated with power generation, chemical petrochemical, aeronautical, aerospace, marine, and nuclear industries. Generally, the oxidation resistance of Inconel alloys depends on the

protective Cr_2O_3 scale exposed to oxidizing atmospheres [8–12]. Many researchers have studied the oxidation characteristics of Inconel 600 and 625.

Xiao et al. [13] investigated the effects of humidity on high-temperature oxidation of the Inconel 600 alloy in terms of oxide layers and residual stress. The NiO and Cr_2O_3 are the main oxides formed during the oxidation between 700 and 900 °C of the Inconel 600 alloy, while only NiO was formed at 600 °C. The NiO and Cr_2O_3 layers were located at external and internal surfaces, respectively. Hashim et al. [14] evaluated the high-temperature oxidation behavior of Inconel 600 and Hastelloy C-22. Both Inconel 600 and Hastelloy C-22 showed the formation of a uniform protective oxide film. The oxide film formed on both alloys was Cr_2O_3 with smaller amounts of $NiCr_2O_4$ spinel. Liu et al. [15] studied the microstructure and oxidation resistance of Inconel 625 superalloy coatings on surfaces of 12CrMoV steel. According to their report, oxygen preferentially reacts with Cr which has high chemical activity in the alloy in the initial oxidation reaction, forming an oxide layer mainly composed of Cr_2O_3 on the surface, which slows down the oxidation reaction. Huang et al. [16] examined the high-temperature oxidation resistance of Inconel 625 alloys fabricated by selective laser melting. They reported that the oxide scale on all samples examined consists of a Cr_2O_3 oxide layer and Ni-rich spinel after oxidation for 40 h at 1000 °C. Sun et al. [17] investigated the high-temperature oxidation behavior and mechanism of an Inconel 625 super alloy fabricated by selective laser melting. Based on the analysis results they obtained, the oxide scales of the samples after oxidation for 100 h are mainly composed of a protective Cr_2O_3 oxide layer with nonprotective Ni-rich oxides inside. Sharifitabar et al. [18] studied the high-temperature oxidation of Inconel 625 fabricated by wire arc additive manufacturing. The results of oxidation testing in the temperature range between 800 and 1000 °C for 20 h showed the formation of Cr_2O_3 and Ni_3Nb phases on the surface of the alloy. At 1100 °C, the oxidation of Ni_3Nb resulted in the formation of $CrNbO_4$ at the oxide/alloy interface. Malafaia et al. [19] studied the microstructure and oxide layer in the isothermal oxidation of the Inconel 625 superalloy at 800 and 1000 °C for 120 and 240 h. The oxide on the surface was identified as predominantly Cr_2O_3 in all conditions, inducing high oxidation resistance. The oxide included spinel $MnCr_2O_4$ at 1000 °C, as well as ABO_4 oxide. Alumina in the internal layer was also observed.

As shown above, the results of existing oxidation studies on 600 and 625 commonly report that Cr_2O_3 is produced as the main oxide, providing improved oxidation resistance. However, the formation of oxides other than Cr_2O_3 varies depending on the oxidation conditions. There is quite a difference between 600 and 625 in terms of chemical composition [3]. The main element, chromium, ranges from 14 to 17 mass% in 600 and from 21 to 24 mass% in 625. Additionally, 600 contains Fe up to 10 mass%, while 625 has limited Fe content with 5 mass% and 8–10 mass%Mo. The constituent oxides and their growth in the oxide scale depend on the composition of the base metal since the concentrations of elements possibly have a significant effect on the continuous diffusion between oxides in the oxide scale and the base metal during long-term oxidation. This study focuses on the examination of the effects of main elements such as Fe and Mo and trace elements less than 1 mass% in addition to Cr on high temperature oxidation from the perspective of the calculated phase diagram.

The purpose of this study is to investigate the effects of main elements on the formation of oxide by examining the oxidation behavior of two alloys, 600 and 625, under the same conditions. The characterization results on oxides formed in the oxide scale were examined by using various types of phase diagrams calculated in the current study. Oxides from trace elements or those that were not clearly observed in the oxide layer, even though they were major elements, were examined by reviewing the calculated phase diagrams and previous studies [13–19].

2. Materials and Methods

The experimental materials examined in this study are Inconel 600 and 625 (as-received). For comparison, the same experiments were conducted on Nickel 201. The

samples used in this study were obtained from VDM Metals (Werdohl, Germany). The chemical compositions of all samples are shown in Table 1 and are based on those of the certificate of analysis provided by the manufacturer. The samples were cut to approximately 2 cm × 2 cm × 2 mm by electrical discharge machining. The surface of samples was ground up to 2000 grade silicon carbide grit sheets. The isothermal oxidation test for all the testing samples was carried out at temperatures of 1000 °C and 1100 °C for 48 h under dry air. According to experimental conditions in the literature reviewed above [6–19], the oxidation test temperature ranged from 800 °C to 1100 °C. In this study, 1100 °C and 1000 °C were selected for the oxidation tests in a high temperature range. Also, considering that the longest holding time at 1100 °C was 40 h, the time was set to 48 h, a slightly longer time. The same holding condition was applied at 1000 °C for comparison. The cross-sectional samples after the oxidation tests were carefully cut and ground with silicon carbide grit sheets and polished with a diamond paste spray (3 and 1 μm). Scanning electron microscope (SEM) was used on the oxidized samples, operating at 20 kV using backscattered electrons (BSEs) imaging mode. Energy dispersive X-ray spectroscopy (EDS) was used to conduct the composition measurement of oxide layers in the cross-section. Electron backscatter diffraction (EBSD) analysis for the oxides on surface was performed using an SEM (SU 8700, HITACHI, Chiyoda, Japan) equipped with EBSD (Velocity ultra, EDAX, Mahwah, NJ, USA). All EBSD maps were examined with respect to crystallographic texture and phase identification using the TSL OIM 8.6 software. The sample was tilted to 70° in the chamber. The operating voltage used was 15 kV to obtain the optimum quality of diffraction patterns. The working distance was 16 mm. The formation of potential oxides at the examined temperatures was investigated based on the phase diagrams calculated by FactSage 8.3, a thermodynamic software package [20]. The databases used were FTlite, which includes all metal elements examined in this study, FToxid, for the oxide phases, and FactPS, for the gas phases.

Table 1. Analyzed compositions of alloy samples examined in this study.

Sample	Analyzed Compositions (mass%)										
	Mo	**Ti**	**Si**	**Mn**	**Cr**	**Cu**	**Co**	**Nb**	**Al**	**Fe**	**Ni**
Nickel 201	-		0.05	0.17	-	0.01	-	-	-	-	Bal.
Inconel 600	-		0.27	0.54	15.42	0.01	0.012	-		8.10	Bal.
Inconel 625	8.10	0.10	0.06	0.05	21.59	0.02	0.15	3.25	0.17	3.45	63.0

3. Results and Discussion

3.1. Oxidation of Nickel 201

Figure 1 shows the phase diagram plotted for oxygen partial pressure and temperature in the Ni-O system calculated by FactSage 8.3. The temperature range in the X-axis includes 1000 and 1100 °C, which are the test temperatures in this study. This result indicates that Ni oxide does not produce any other types of oxides other than monoxide. Figure 2 displays the images of cross-sections by SEM−back scattered electron (BSE) in Nickel 201 samples oxidized for 48 h at 1000 and 1100 °C, respectively. Cross-sections of Nickel 201 oxidized with different temperatures seem to be similar only in contrast according to BSE. The base metal and the oxide layer are clearly distinguished, and the oxide layer shows that it has grown horizontally and neatly. However, it appears that the oxide layer grew thicker even with a temperature difference of about 100 °C. Additionally, as shown in Figure 2c, the oxide particles are distributed along the grain boundaries in the base metal right under the oxide layer. The composition by SEM-EDS for Area 1 in Figure 2c is shown in Table 2. From this result, it is confirmed that those particles are oxides. Figure 3 shows the EBSD results of Nickel 201 oxidized at 1000 and 1100 °C for 48 h. The oxide layer of Nickel 201 was found to be NiO, as shown in Figure 1, and can be divided into upper and lower layers based on crystallographic analysis results in Figure 3b. The lower layer consisted of relatively fine, equiaxed oxide crystals, while the upper layer showed the oxide crystals

with columnar structures that grow long in the thickness direction. According to a previous study [21], the NiO crystals with both elongated and equiaxed shapes in the oxidation of Ni were observed, simultaneously, as in this study. As the temperature rises by 100 °C, it can be seen that the oxide layer thickness has increased, and, in particular, the area with the columnar structure has grown noticeably. A study on the oxidation of a nickel-based superalloy also showed that the oxides with the columnar structure were associated with a fast diffusion of oxygen [22]. Therefore, it appeared that the growth of oxide crystals in the thickness direction possibly led to the acceleration of the oxidation.

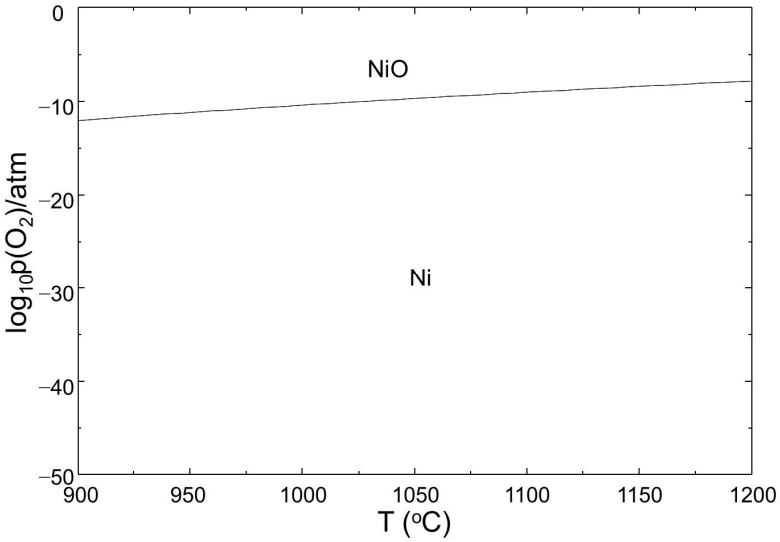


Figure 1. Phase diagram plotted for O_2 partial pressure and temperature in Ni-O system calculated by FactSage 8.3 [20].

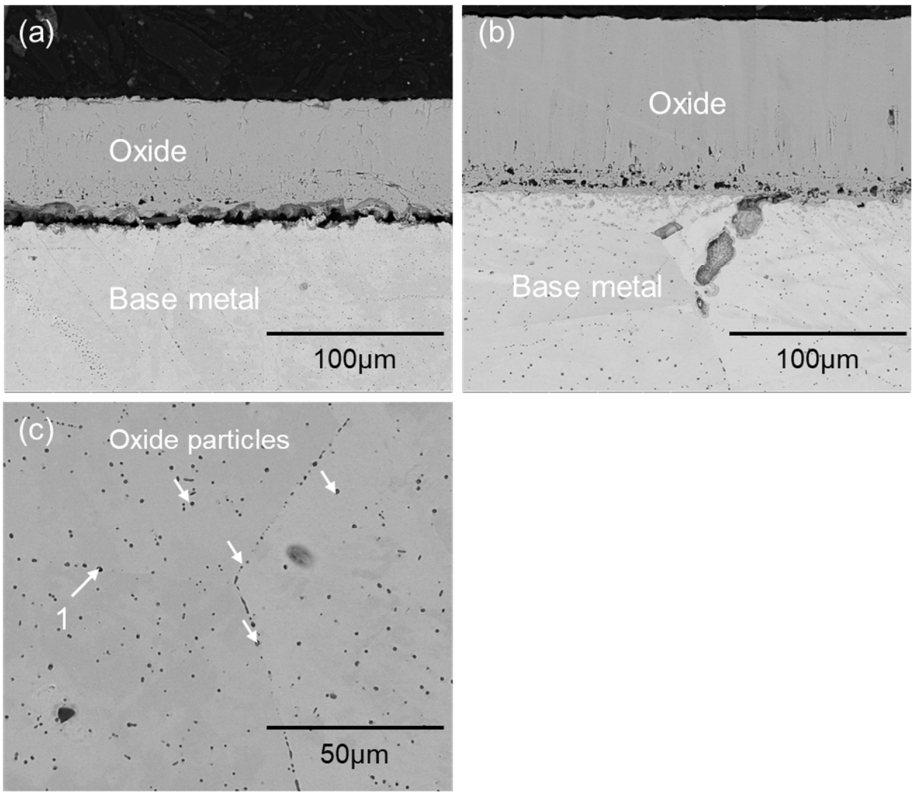


Figure 2. SEM-BSE images on the cross-sections of Nickel 201 sample oxidized for 48 h at (**a**,**c**) 1000 °C and (**b**) 1100 °C. The numbers in the images correspond to the areas analyzed by EDS.

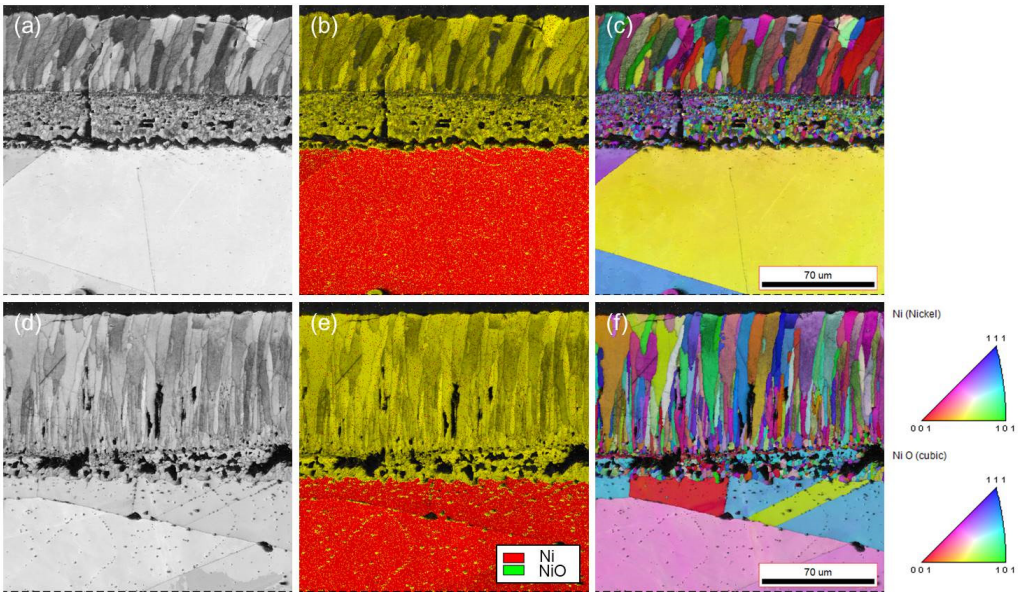


Figure 3. EBSD results of Nickel 201 oxidized for 48 h. (**a**) Image quality (IQ) map, (**b**) phase map, and (**c**) IQ + Inverse pole figure (IPF) map at 1000 °C. (**d**) IQ map, (**e**) phase map, and (**f**) IQ + IPF map at 1100 °C.

3.2. Oxidation of Inconel 600

Figure 4 shows the formation of oxides according to the main elements in the oxidation reaction for Inconel 600. These are calculated by excluding the alloying elements shown in Table 1 that are less than about 1 mass%. The equilibrium oxide phases according to the oxygen partial pressure are shown on the Y-axis. Oxide does not exist in the area where the oxygen partial pressure on the Y-axis is lowest. However, as the oxygen partial pressure increases, the regions containing the presence of oxides begin to appear. The primary oxide in the region, including the oxide that first appeared, is Cr_2O_3. It can be said that the oxides produced in the regions with lower oxygen partial pressure have priority in the oxidation process. Therefore, in those phase diagrams, it can be seen that Cr_2O_3 is the preferentially produced oxide. The oxide that appears after Cr_2O_3 is spinel because the Ni matrix becomes relatively Cr-poor due to the formation of Cr_2O_3. As the oxygen partial pressure further increases, a region appears where Cr_2O_3 is absent and only spinel and Ni exist, followed by a region where only monoxide and spinel exist. This region represents when the entire alloy is in equilibrium with oxygen and assumes that the entire alloy has formed oxides. As in various Ni-based alloys with oxidation resistance, it is thought that Cr_2O_3 is the preferentially produced oxide in the case of Inconel 600. The spinel exists in all the ranges of variables on the X-axis. In this case, the spinel contains both $NiCr_2O_4$ and $FeCr_2O_4$, and as the Fe content increases, the presence of $FeCr_2O_4$ in spinel increases. It can be explained that the formation of Cr_2O_3 and two types of spinel lowers the Cr and Fe content in the base metal, eventually leading to the formation of monoxide. Figure 4b shows the production of oxide according to changes in the Cr content with the Fe content fixed. This does not show a significant difference in terms of the produced oxide compared to those in Figure 4a. Therefore, it can be seen that there is no significant difference in the produced oxides within the range of the main alloying elements in Inconel 600. As shown in Figure 4c, no significant changes were observed depending on temperature changes. Figure 5 shows the cross-sections of the Inconel 600 alloy oxide layer observed by SEM-BSE. Curved oxide layers exist on the base metals and have grown thicker as the temperature increases by 100 °C. However, it can be seen that the thickness of the oxide layer, which is considered Cr_2O_3, is much thinner compared to that of Nickel 201 mentioned above. Therefore, it can be said that Cr_2O_3 acts as a protective film, as revealed through previous studies. As a result of SEM-EDS analysis, as shown in Table 2, the oxide layer is believed to be Cr_2O_3

and contains trace amounts of Mn or Ti, as shown in the compositions for Areas 3, 5 and 6. These are the trace elements added to Inconel 600 covered in this study. Even though they are added in trace amounts, they look to have a strong tendency for surface segregation. In addition, Area 6 was enriched in Ni and Fe compared to Area 5. Therefore, it is thought that Ni-based and Fe-based spinels exist in the oxide layer, as in the phase diagram shown above. The Cr content in Areas 7 and 8, which is lower than that in the base metal region, is thought to be associated with Cr loss by Cr_2O_3 formation. In particular, the Fe content is much higher than that of the matrix. From this result, it can be seen that the tendency of Fe surface segregation in Inconel 600 is quite noticeable. Figure 6 shows the EBSD results for the cross-sections shown in Figure 5. The oxide layer of Inconel 600 is composed of equiaxed oxide crystals at both 1000 and 1100 °C. Additionally, the main oxides were found to be Cr_2O_3, and some NiO was also observed at the interface with the base metal. This is considered to be caused by a lack of Cr at the interface due to the formation of Cr_2O_3. Besides this, the existence of Fe-based spinel was not discovered. Other oxides are possibly present in the form of small particles within the oxide layer, but were not observed due to the limit in the resolution of EBSD based on SEM. However, the results indicate that the oxide layer is composed of equiaxed oxide particles when it is protective. According to the report from Hashim et al. [14], the oxide phase analysis showed the presence of Cr_2O_3 and some spinel oxide $NiCr_2O_4$, which were detected from all examined oxide scales on Inconel 600, while No NiO was detected, which may be due to the small thickness. The presence of Cr_2O_3 in the previous report [14] is consistent with the results of this study, but Ni-based spinel was not observed in this study. Xiao et al. [13] reported that the NiO and Cr_2O_3 in Inconel 600 were the main oxides formed during oxidation at 700 to 900 °C and only NiO was formed at 600 °C. The NiO and Cr_2O_3 were located at the external surface and internal surface, respectively. And also, the presence of spinel was observed in their analysis, but it was not mentioned as the main oxide. Therefore, based on the above results, spinel, which is an intermediate oxide between NiO and Cr_2O_3, is formed during the oxidation of Inconel 600, but it is not the major oxide. NiO appears to be dominant when oxidation conditions are not relatively harsh. Conversely, the more severe the oxidation conditions, the more dominant Cr_2O_3 becomes. Meanwhile, the presence of NiO in the outermost layer is different from that in the present study. As mentioned earlier, this is considered to be because the presence of NiO becomes dominant as the conditions in terms of the oxidation time and temperature become less severe. However, it is thought that the Cr_2O_3 in the oxide scale becomes increasingly dominant and the external NiO disappears as the oxidation continues.

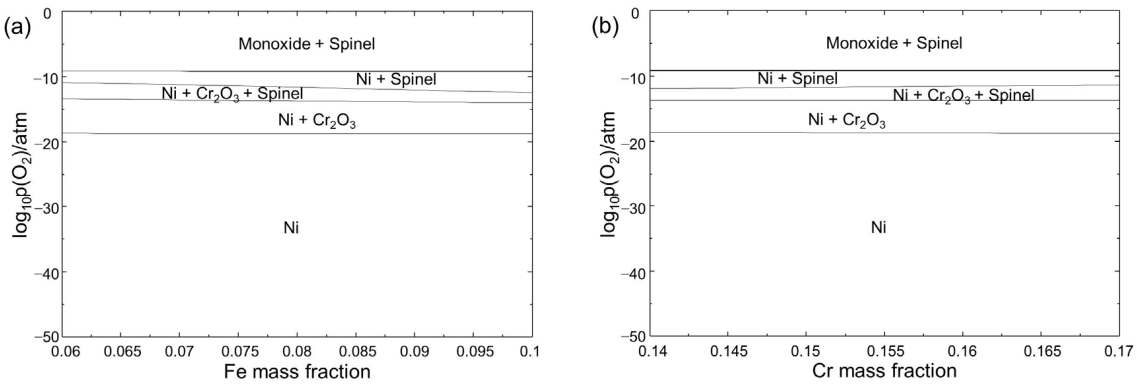


Figure 4. *Cont.*

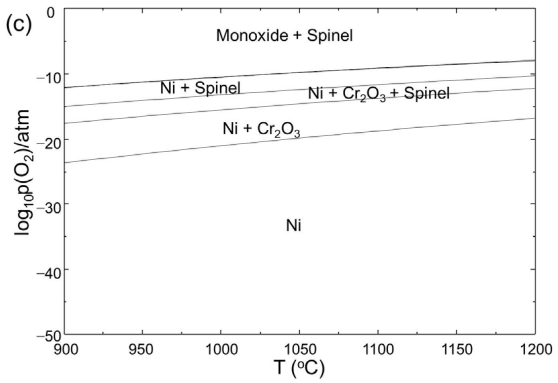


Figure 4. Phase diagrams plotted for (**a**) O_2 partial pressure and Fe mass fraction, (**b**) O_2 partial pressure and Cr mass fraction at 1100 °C, and (**c**) O_2 partial pressure and temperature in Ni-Cr-Fe-O system calculated by FactSage 8.3 [20]. The fixed content of each element is the same as that of Inconel 600 in Table 1. To simplify calculations, the elements less than 1 mass% are excluded.

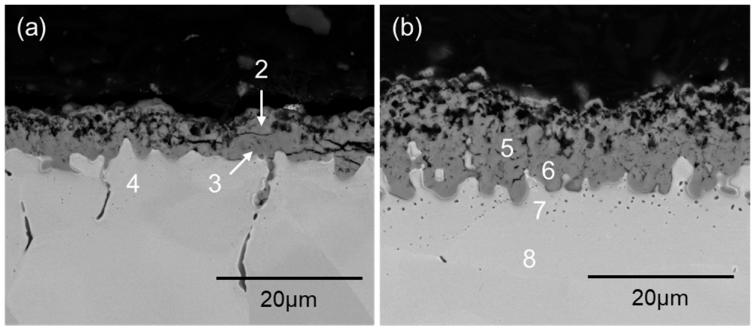


Figure 5. SEM−BSE images on the cross-sections of Inconel 600 sample oxidized for 48 h at (**a**) 1000 °C and (**b**) 1100 °C. The numbers in the images correspond to the areas analyzed by EDS.

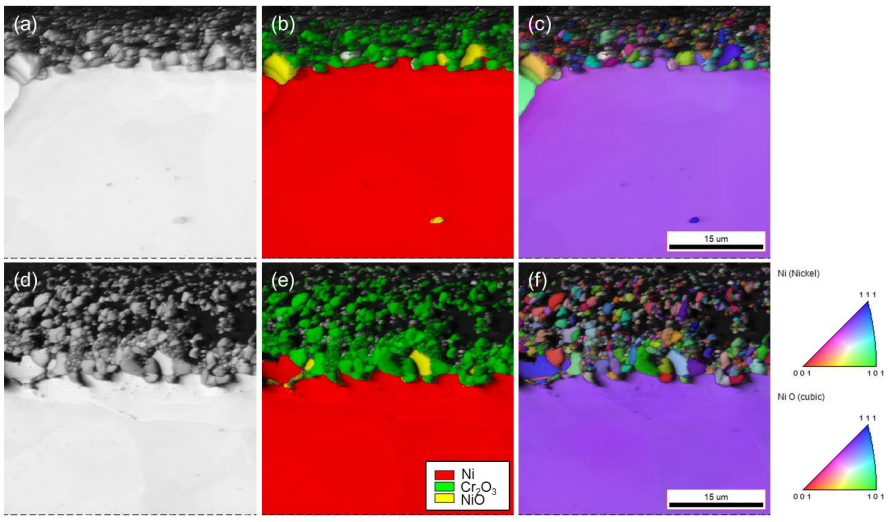


Figure 6. EBSD results of Inconel 600 oxidized for 48 h. (**a**) Image quality (IQ) map, (**b**) phase map, and (**c**) IQ + Inverse pole figure (IPF) map at 1000 °C. (**d**) IQ map, (**e**) phase map, and (**f**) IQ + IPF map at 1100 °C.

3.3. Oxidation of Inconel 625

Figure 7 shows the formation of oxides depending on the contents of major elements in the oxidation for Inconel 625. As shown in Figure 4 above, they are the phase diagrams calculated after excluding the elements of less than 1 mass%. As shown in Figure 7a, the region appeared where the Cr_2O_3 preferentially forms as the primary oxide as the oxygen partial

pressure increases. The oxidation after Cr_2O_3 would be proceeded with the formation of Nb_2O_5. Therefore, in the case of Inconel 625 containing Nb, it is thought that when Cr is consumed due to Cr_2O_3, the surface segregation of Nb becomes relatively more prominent. After the Nb_2O_5 formation, spinel and monoxide are shown to be formed, similarly to those in Inconel 600. And then, the oxidation of Inconel 625 is followed by the MoO_2 formation since it also contains a certain amount of Mo. However, when the oxygen partial pressure further increases, the MoO_2 becomes a gas. This is thought to be caused by the evaporation temperature being lower than the oxidation temperature as the MoO_2 becomes MoO_3. Figure 7b,c also show that there is no significant change in the oxide production as the content of other elements changes, while only a fraction of each oxide is different. In addition, as shown in Figure 7d, there is no significant change in the oxide formation as the temperature increases, but the only change is that the MoO_3 is present rather than gas at approximately 900 °C. Figure 8 shows the SEM-BSE images on the cross-section of the oxide layer of the Inconel 625 alloy oxidized at 1000 and 1100 °C. The morphology of the oxide layer appears to be similar to that of Inconel 600, and there is no significant difference between Inconel 600 and 625 in the thickness of the oxide layer. As shown in Table 2, the composition analysis on Areas 9 and 10 indicated that Cr-rich oxide was formed on the surfaces, and Area 9 also contains a trace amount of Si. Considering that the Si content in the Inconel 625 used in this study is 0.06 mass%, it can be seen that the Si has a strong tendency to surface segregate. Although the Mo is enriched in Areas 11 to 13, it was not detected in the oxide layers, which appears to be related to the formation of MoO_3, as mentioned in the phase diagrams above, and its vaporization temperature being lower than the test temperatures. In addition, Nb was detected only in 11, right below the oxide layer, and was not present inside. This is thought to be caused by Nb loss due to continuous surface segregation under harsh oxidation conditions. At 1100 °C, a trace amount of Al was also detected in Area 14, which corresponds to the Cr_2O_3 oxide layer. In addition, the existence of an intermediate oxide layer between the Cr_2O_3 oxide layer and the base metal was found as the oxide layer grew, as indicated by Area 15. This intermediate oxide layer was found to be Nb-rich and also contained Ti. Area 15 possibly corresponds to a mixture of several oxides, mainly including the Nb-based oxide shown in the phase diagrams above. In Area 16, which corresponds to the base metal right below the oxide layer, a Mo content much higher than that at 1000 °C was detected. Therefore, it was considered that the surface segregation of Mo was further accelerated as the temperature increased. Huang et al. [14] found the presence of Al_2O_3 and TiO_2 oxides as a result of internal oxidation caused by oxygen diffusion into the interior. The Al-based and Ti-based oxides are found not only in the base material but also possibly inside the oxide layer, as in this study. In the study of Sun et al. [17], the phase analysis on the oxide scale of Inconel 625 showed that it is mainly composed of Cr_2O_3 with Ni-rich oxides inside. Malafaia et al. [19] discovered the existence of spinel oxide related to Mn in addition to Cr_2O_3. Additionally, they also observed the presence of aluminum oxides formed through internal oxidation in the base metal. Figure 9 shows the EBSD results for the cross-section of the oxide layer shown in Figure 8. Similarly to Inconel 600, the presence of a Cr_2O_3 oxide layer composed of fine equiaxed oxide particles was observed, and the size of these particles appears to become coarsened as the oxidation temperature increases. The presence of other oxides was not detected, and, in particular, the entire oxide layer was not separated into Cr_2O_3 and the intermediate layer. This is possibly due to the characteristic of the EBSD technique, which analyzes the sample by tilting it by about 70°.

Table 2. Analyzed compositions of areas numbered in Figures 2, 5 and 8 by SEM-EDS.

Area	Analyzed Compositions (at%)									
	Ni	Cr	Si	Mn	Fe	Ti	Mo	Nb	Al	O
1	57.3	-	-	-	-	-	-	-	-	42.7
2	-	57.3	-	-	-	-	-	-	-	42.7
3	-	61.7	-	0.8	-	-	-	-	-	37.5
4	79.0	10.8	-	-	10.2	-	-	-	-	-
5	-	55.5	-	-	-	0.8	-	-	-	43.8
6	9.3	42.9	1.8	-	1.6	0.7	-	-	-	43.8

Table 2. *Cont.*

Area	Analyzed Compositions (at%)									
	Ni	**Cr**	**Si**	**Mn**	**Fe**	**Ti**	**Mo**	**Nb**	**Al**	**O**
7	79.4	10.1	-	-	10.5	-	-	-	-	-
8	78.5	9.7	1.3	-	10.5	-	-	-	-	-
9	-	51.1	1.7	-	-	-	-	-	-	47.2
10	-	53.7	-	-	-	-	-	-	-	46.3
11	62.4	13.2	-	-	3.7	-	5.2	3.1	-	12.5
12	76.6	11.4	-	-	4.6	-	7.4	-	-	-
13	75.4	12.9	-	-	4.4	-	7.3	-	-	-
14	-	53.7	-	-	-	-	-	-	0.9	45.4
15	9.2	15.6	-	-	-	1.8	-	29.4	-	44.0
16	77.7	9.2	-	0.4	4.9	-	7.8	-	-	-

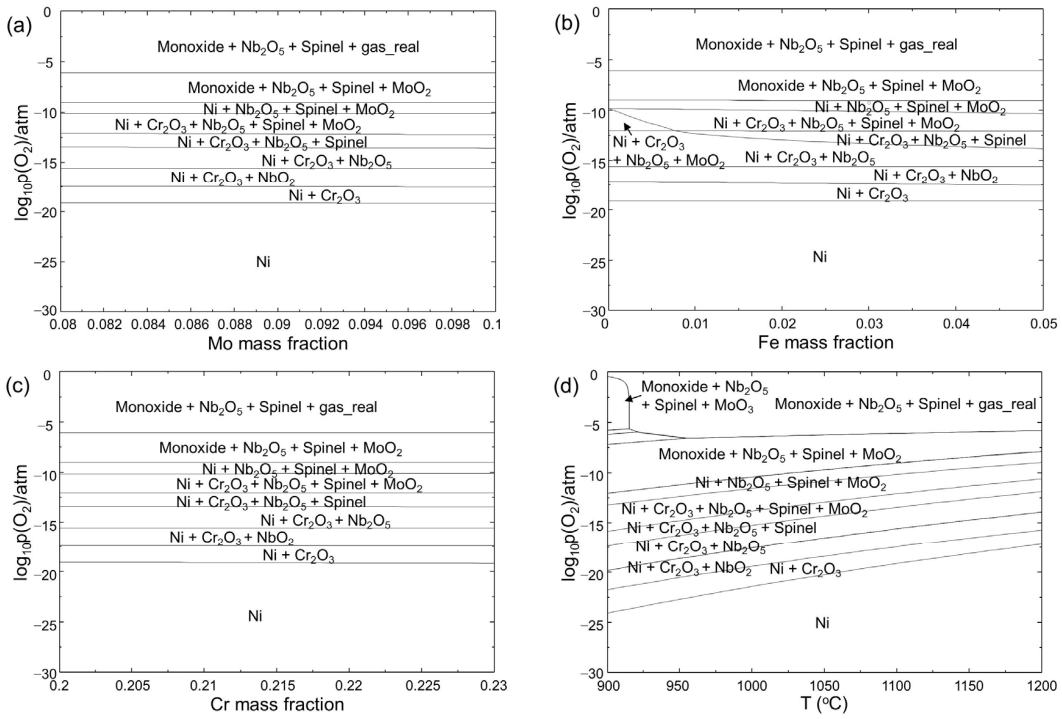


Figure 7. Phase diagrams plotted for (**a**) O_2 partial pressure and Mo mass fraction, (**b**) O_2 partial pressure and Fe mass fraction, (**c**) O_2 partial pressure and Cr mass fraction at 1100 °C, and (**d**) O_2 partial pressure and temperature in Ni-Cr-Mo-Nb-Fe-O system calculated by FactSage 8.3 [20]. The fixed content of each element is the same as that of Inconel 625 in Table 1. To simplify calculations, the elements less than 1 mass% are excluded.

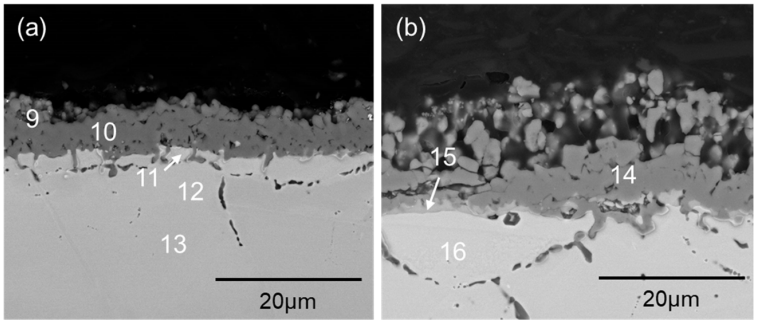


Figure 8. SEM-BSE images on the cross-sections of Inconel 625 sample oxidized for 48 h at (**a**) 1000 °C and (**b**) 1100 °C. The numbers in the images correspond to the areas analyzed by EDS.

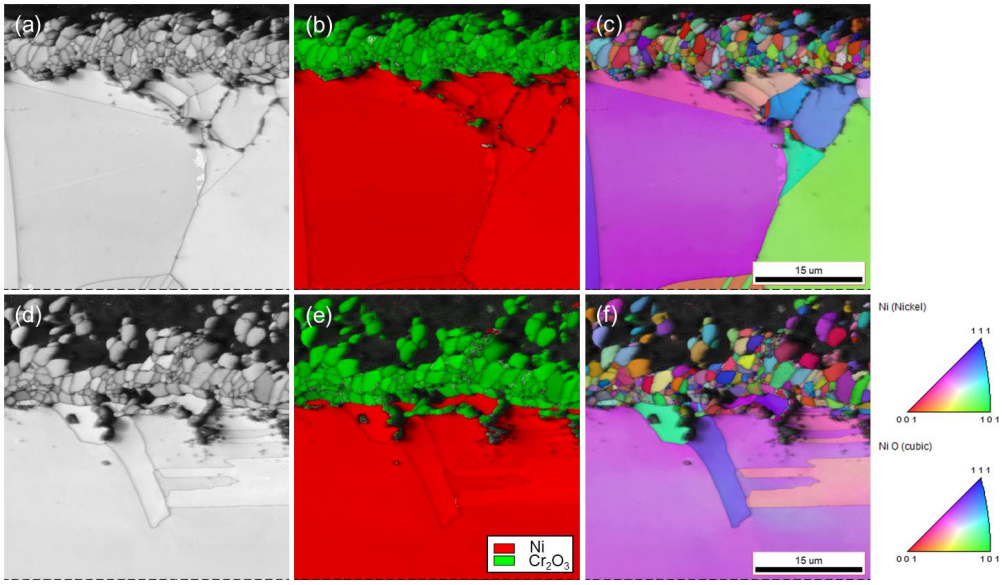


Figure 9. EBSD results of Inconel 625 oxidized for 48 h. (**a**) Image quality (IQ) map, (**b**) phase map, and (**c**) IQ + Inverse pole figure (IPF) map at 1000 °C. (**d**) IQ map, (**e**) phase map, and (**f**) IQ + IPF map at 1100 °C.

3.4. Interaction Between Main Oxides and Alloying Elements in Oxidation

From the results of the two types of Inconel alloys examined in this study, it was found that the oxide layers mainly composed of Cr_2O_3 were formed. Therefore, examinations on the intermediate products between Cr_2O_3 and each Inconel alloy matrix can help predict the interactions between the oxide layer and the matrix during long-term oxidation. Figure 10 shows the equilibrium products between Inconel 600 and 625 matrixes and Cr_2O_3 at each oxidation temperature. It can be seen that each base metal does not form any intermediate products with Cr_2O_3. Therefore, the oxides present at the interface between Cr_2O_3 and the base metals observed in this study may not have been formed by the interaction between those two phases. On the other hand, in the case of NiO rather than Cr_2O_3, oxides such as spinel, which were mentioned in the previous studies reviewed in this study, can be produced on the NiO-rich side, as shown in Figure 11. As mentioned above, according to the research by Xiao et al. [13], only NiO was observed at low temperatures, and NiO existed on the external layer and Cr_2O_3 existed on the internal layer as the temperature increases. Based on this result, if the oxidation temperature is low, the NiO may be the main oxide. However, even at high temperatures, the NiO possibly dominates the oxide layer in the early stages of oxidation. It is thought that oxides such as spinel are produced by the interaction between the NiO and the base metals. However, as oxidation continues, it is assumed that the main oxide changes to Cr_2O_3 due to the continued surface segregation of Cr from the matrix. This is contradictory to the hypothesis that the Cr_2O_3 is the preferential oxide, as shown in Figures 4 and 7. The oxide formation in those phase diagrams can be explained assuming that the base metal is in the equilibrium at each temperature, and the microstructure heterogeneity and heating process to the target temperature should be controlled to explain the actual oxidation. Therefore, it is thought that there may be conditions under which NiO can still exist as the main oxide. In a previous study [23], the initial oxidation of an alloy sample did not follow that of the equilibrium phase diagram including oxygen partial pressure, but as oxidation continued for a long time, it began to exhibit oxidation behavior similar to that of the phase diagram. Figure 12 shows the relationship between trace elements that were not included in the phase diagram calculations and Cr_2O_3. These elements were detected in the oxide layer even though they were in trace amounts in previous studies. In the case of Mn, it can be seen that it forms a Mn-based spinel in relation to Cr_2O_3, and Si, Al, and Ti are confirmed to form SiO_2,

Al_2O_3, and Ti_2O_3, respectively. All of these oxides were frequently observed in previous studies. In this study, they were also detected in the oxide layer, and it appears that the aforementioned oxides are formed due to their strong surface segregation and reaction with Cr_2O_3 depending on the duration of oxidation.

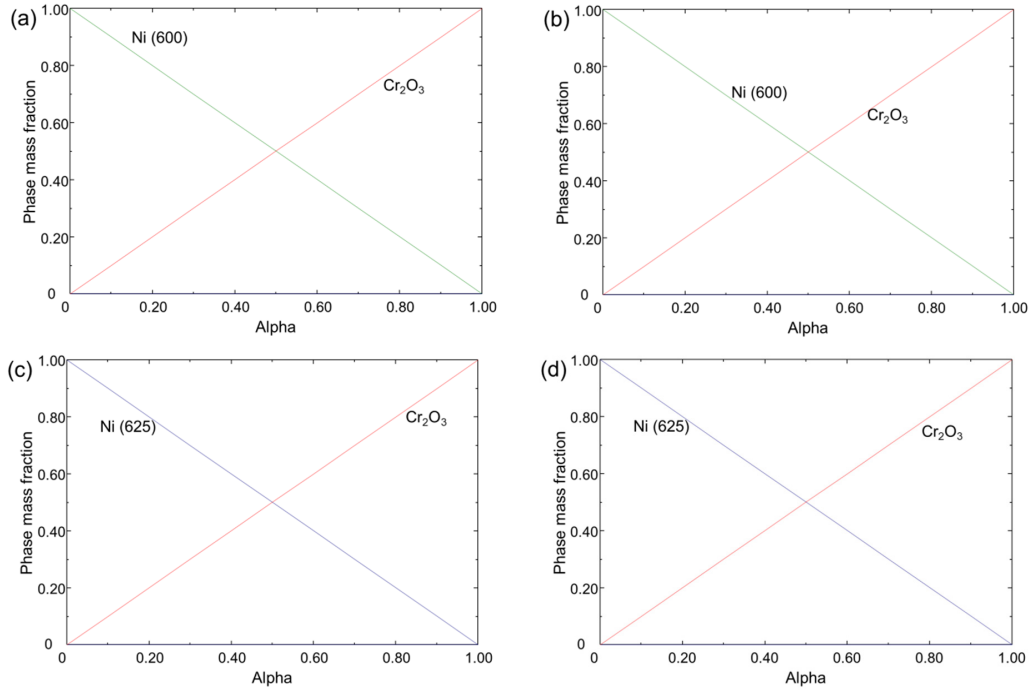


Figure 10. Equilibrium products according to the relative fraction between Ni base metals and Cr_2O_3 calculated by FactSage 8.3 [20]. (**a**,**c**) 1000 °C and (**b**,**d**) 1100 °C. To simplify calculations, the elements less than 1 mass% are excluded.

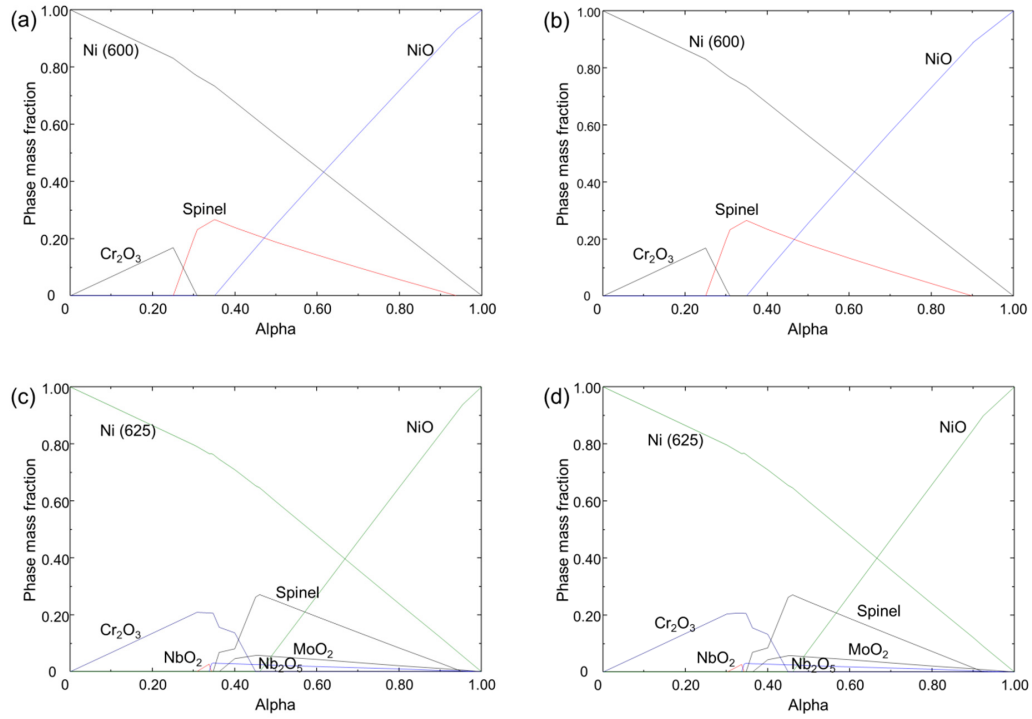


Figure 11. Equilibrium products according to the relative fraction between Ni base metals and NiO calculated by FactSage 8.3 [20]. (**a**,**c**) 1000 °C and (**b**,**d**) 1100 °C. To simplify calculations, the elements less than 1 mass% are excluded.

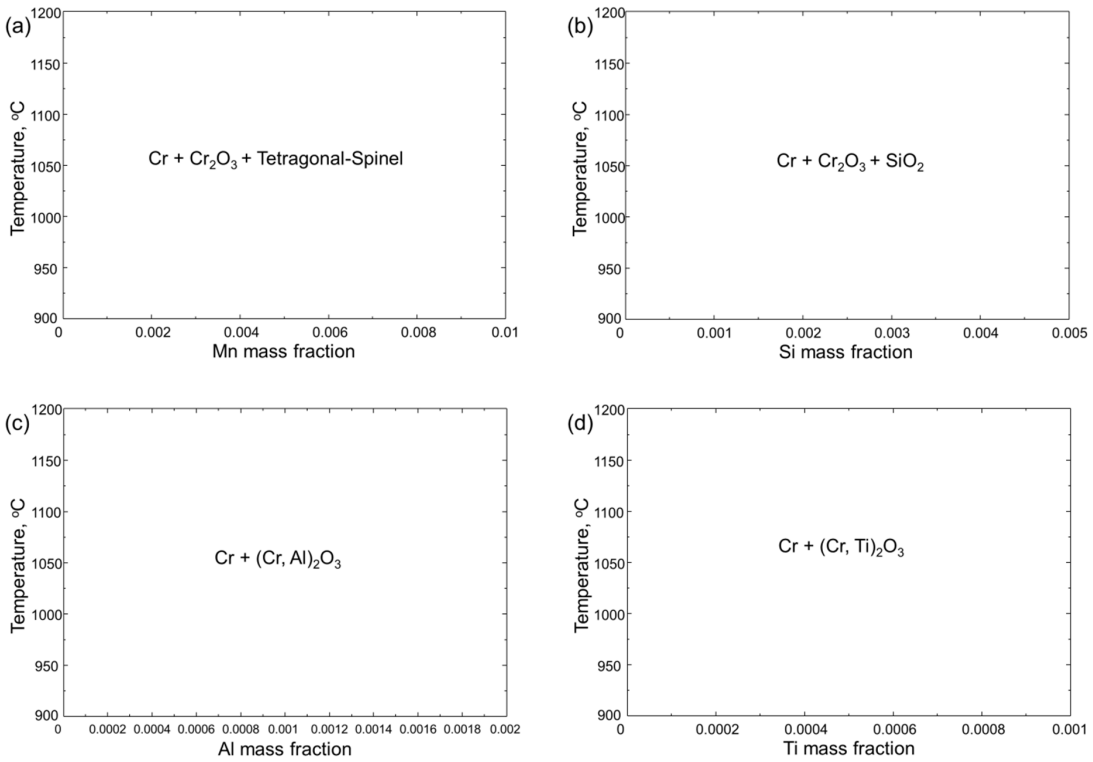


Figure 12. Phase diagrams plotted for temperature and (**a**) Mn mass fraction, (**b**) Si mass fraction, (**c**) Al mass fraction, and (**d**) Ti mass fraction in Cr_2O_3—Elements with trace concentrations (below 1 mass% in Table 1) calculated by FactSage 8.3 [20].

4. Conclusions

As a result of isothermal oxidation tests at 1000 and 1100 °C for 48 h, it was seen that the NiO layer on Nickel 201 was significantly grown. The NiO layer with a columnar structure mainly led to the rapid growth of the oxide layer. On the other hand, two Inconel alloys, 600 and 625, showed significantly thinner oxide layers than that of Nickel 201, which were confirmed to be mainly composed of Cr_2O_3. It was also shown that the Cr_2O_3 layer was composed of equiaxed and fine oxide crystals. In the oxidation of Inconel 625, an intermediate oxide layer was found at the interface between Cr_2O_3 and the base metal. This is thought to be because the 625 alloy contains a greater amount of third elements (Mo, Nb, etc.) in addition to Cr. The results of the oxide layer analyses under the conditions in this study showed that elements other than Cr did not have a significant effect on the formation of the oxide layer. Based on the SEM-EDS results, it is believed that the Cr_2O_3 layer contains spinel phases formed from Fe, as one of the main alloying elements, and trace additive elements such as Mn. From the phase diagrams with oxygen partial pressure calculated by FactSage 8.3, the distribution of alloying elements in and around the oxide layers and the presence of oxides composed of those elements, which were found and mentioned not only in the results in this study but also in previous studies, could be explained. In addition, based on the results in the current study and previous studies, it is suggested that the main oxide of Inconel alloys is Cr_2O_3, but NiO may be the main oxide at low temperatures and at the initial oxidation at high temperatures, and that in the meantime, spinel, etc., may be formed through the interaction between NiO and alloying elements in the base metal.

Author Contributions: Conceptualization: S.-H.H.; methodology: S.-H.H.; Data curation: J.C., D.-H.K. and S.-H.H.; writing—review and editing: S.-H.H.; supervision: D.-H.K. All authors have read and agreed to the published version of the manuscript.

Funding: This research received no external funding.

Institutional Review Board Statement: Not applicable.

Informed Consent Statement: Not applicable.

Data Availability Statement: Available upon request from the corresponding author.

Acknowledgments: This study has been conducted with the support of the Ministry of Trade, Industry and Energy as "Transportation Equipment Technology Development Program (00256056)".

Conflicts of Interest: The authors declare that the research was conducted in the absence of any commercial or financial relationships that could be construed as a potential conflict of interest.

References

1. Kofstad, P.; Rahmel, A.; Rapp, R.A.; Douglas, D.L. International workshop on "New Fundamentals of Scale Growth". *Oxid. Met.* **1989**, *32*, 125–166. [CrossRef]
2. Reed, R.C. *The Superalloys: Fundamentals and Applications*; Cambridge University Press: London, UK, 2006.
3. Buddaraju, K.M.; Sastry, G.R.K.; Kosaraju, S. A review on turning of Inconel alloys. *Mater. Today Proc.* **2021**, *44*, 2645–2652. [CrossRef]
4. Moulin, P.; Huntz, A.M.; Lacombe, P. Influence des phenomenes diffusionnels sur le mecanisme d'oxydation des alliages Ni Cr. *Acta Metall.* **1980**, *28*, 745–756. [CrossRef]
5. Moulin, G.; Huntz, A.M.; Rousselet, J.M. Stresses associated with Inconel 600 oxidation. *Mater. Sci. Eng. A* **1989**, *120*, 221–228. [CrossRef]
6. Paul, C.P.; Ganesh, P.; Mishra, S.K.; Bhargava, P.; Negi, J.; Nath, A.K. Investigating laser rapid manufacturing for Inconel-625 components. *Opt. Laser Technol.* **2007**, *39*, 800–805. [CrossRef]
7. Shankar, V.; Rao, K.B.S.; Mannan, S.L. Microstructure and mechanical properties of Inconel 625 superalloy. *J. Nucl. Mater.* **2001**, *288*, 222–232. [CrossRef]
8. Ma, S.; Ding, Q.; Wei, X.; Zhang, Z.; Bei, H. The Effects of Alloying Elements Cr, Al, and Si on Oxidation Behaviors of Ni-Based Superalloys. *Materials* **2022**, *15*, 7352. [CrossRef]
9. Alano, J.H.; Siqueira, R.L.; Martins Júnior, C.B.; Silva, R.; Vacchi, G.d.S.; Rovere, C.A.D. A Survey on the Oxidation Behavior of a Nickel-Based Alloy Used in Natural Gas Engine Exhaust Valve Seats. *Metals* **2023**, *13*, 49. [CrossRef]
10. Singh, P.; Singh, S.; Singh, H.; Calla, E.; Grewal, H.S.; Arora, H.S.; Krishnamurthy, A. Characterization and High-Temperature Oxidation Behavior of Ni–20Cr Deposits Fabricated by Cold Spray-Based Additive Manufacturing. *Coatings* **2023**, *13*, 904. [CrossRef]
11. Park, S.-J.; Seo, S.-M.; Yoo, Y.-S.; Jeong, H.-W.; Jang, H. Effects of Cr, W, and Mo on the High Temperature Oxidation of Ni-Based Superalloys. *Materials* **2019**, *12*, 2934. [CrossRef]
12. Lei, P.; Zhou, L.; Zhang, Y.; Wang, F.; Li, Q.; Liu, J.; Xiang, X.; Wu, H.; Wang, W.; Wang, F. Corrosion Behavior of Ni-Cr Alloys with Different Cr Contents in NaCl-KCl-$MgCl_2$. *Materials* **2024**, *17*, 2335. [CrossRef] [PubMed]
13. Xiao, J.; Prud'homme, N.; Li, N.; Ji, V. Influence of humidity on high temperature oxidation of Inconel 600 alloy: Oxide layers and residual stress study. *Appl. Surf. Sci.* **2013**, *284*, 446–452. [CrossRef]
14. Hashim, A.A.; Hammood, A.S.; Hammadi, N.J. Evaluation of High-Temperature Oxidation Behavior of Inconel 600 and Hastelloy C-22. *Arab. J. Sci. Eng.* **2015**, *40*, 2739–2746. [CrossRef]
15. Liu, F.; Gao, X.; Zeng, Z.; You, Q.; Liu, F.; Wang, Z.; Xu, Y.; Zheng, H.; Liu, Q.; Lin, X.; et al. Comparative study on microstructure and oxidation resistance of Inconel 625 superalloy coatings on 12CrMoV steel surfaces prepared by CMT and MIG cladding. *J. Mater. Res. Technol.* **2024**, *29*, 3910–3922. [CrossRef]
16. Huang, W.; Li, Y.; Yanjie, R.E.N.; Sun, J.; Xia, Z.; Zhou, L.; Li, C.; Chen, J.; Niu, Y.; Zhao, Y. Effect of scanning speed on the high-temperature oxidation resistance and mechanical properties of Inconel 625 alloys fabricated by selective laser melting. *Vacuum* **2022**, *206*, 111447. [CrossRef]
17. Sun, Y.; Chen, L.; Li, L.; Ren, X. High-temperature oxidation behavior and mechanism of Inconel 625 super-alloy fabricated by selective laser melting. *Opt. Laser Technol.* **2020**, *132*, 106509. [CrossRef]
18. Sharifitabar, M.; Khorshahian, S.; Afarani, M.S.; Kumar, P.; Jain, N.K. High-temperature oxidation performance of Inconel 625 superalloy fabricated by wire arc additive manufacturing. *Corros. Sci.* **2022**, *197*, 110087. [CrossRef]
19. Malafaia, A.M.S.; Oliveira, R.B.; Latu-Romain, L.; Wouters, Y.; Baldan, R. Isothermal oxidation of Inconel 625 superalloy at 800 and 1000 °C: Microstructure and oxide layer characterization. *Mater. Charact.* **2020**, *161*, 110160. [CrossRef]
20. Bale, C.W.; Bélisle, E.; Chartrand, P.; Decterov, S.A.; Eriksson, G.; Gheribi, A.E.; Hack, K.; Jung, I.H.; Kang, Y.B.; Melançon, J.; et al. FactSage thermochemical software and databases, 2010–2016. *Calphad* **2016**, *54*, 35–53. [CrossRef]
21. Xi, X.; Shen, Z.; Zhang, J.; Gleeson, B.; Young, D.J. Nickel oxide scale microstructure and accelerated growth in combustion flue gas: Effect of ash particles. *Corros. Sci.* **2023**, *218*, 111153. [CrossRef]
22. Min, S.L.; Zhang, H.W.; Liu, H.; He, L.H.; Qiu, S.Y.; Chu, F.Z.; Huang, S.S.; Wang, Y.Q.; Zhang, K.; Liang, J.J.; et al. Oxidation kinetic behavior and microstructure mechanism of GH3536 alloy fabricated by laser powder bed fusion. *npj Mater. Degrad.* **2023**, *7*, 83. [CrossRef]
23. Ha, S.H.; Yoon, Y.O.; Kim, B.H.; Lim, H.K.; Lim, S.H.; Kim, S.K. Oxide scale behavior of Al–7.5 mass%Mg alloy containing trace Ca during short-term oxidation. *Mater. Express* **2021**, *11*, 1881–1886. [CrossRef]

Disclaimer/Publisher's Note: The statements, opinions and data contained in all publications are solely those of the individual author(s) and contributor(s) and not of MDPI and/or the editor(s). MDPI and/or the editor(s) disclaim responsibility for any injury to people or property resulting from any ideas, methods, instructions or products referred to in the content.